Optics and Lasers in Engineering 159 (2022) 107228

Contents lists available at ScienceDirect

Optics and Lasers in Engineering

journal homepage: www.elsevier.com/locate/optlaseng

Complex-domain SVD- and sparsity-based denoising for optical diffraction tomography☆

Igor Shevkunov[a,1,2,*], Michał Ziemczonok[b,3], Małgorzata Kujawińska[b,4], Karen Egiazarian[a,5]

[a] Tampere University, Faculty of Information Technology and Communication Sciences, Tampere, Finland
[b] Warsaw University of Technology, Institute of Micromechanics and Photonics, Warsaw, Poland

ARTICLE INFO

Keywords:
Noise filtering
Noise in imaging systems
Tomographic imaging
Optical diffraction tomography
Refractive index reconstruction
Singular value decomposition
Sparse representation

ABSTRACT

In this paper, we adopt a complex-domain cube filter (CCF) developed for hyperspectral 3D complex domain images for noise suppression of 3D complex-valued data in optical diffraction tomography. CCF is based on two processing steps: singular value decomposition (SVD) and complex-domain sparsity-based filter (CDID). SVD provides data compression and CDID noise suppression in the compressed domain. We demonstrate that the CCF algorithm can be used to denoise captured projections (sinogram), which results in enhanced tomographic reconstruction. The accuracy and quantitative advantage of CCF application are shown in simulation tests and in the processing of the experimental data. We show that the algorithm effectively suppresses noise and retrieves objects' details even for highly noisy data.

1. Introduction

Tomography is a method of 3D image reconstruction of an object through the use of any kind of penetrating wave [1]. There are over 20 types of tomographic systems that rely on electromagnetic radiation. They operate in various parts of the spectrum, starting from x-ray [2] and gamma radiation [3] and up to terahertz wavelengths [4]. The current paper is devoted to optical diffraction tomography (ODT) [5], where radiation is in the visible part of the spectrum and 3D imaging is enabled by the projections acquired using digital holography. ODT is successfully used in a wide range of applications but currently excels in biomedical imaging, as it is a high-resolution, noninvasive and quantitative technique. ODT reconstruction provides a 3D matrix of the refractive index (RI) distribution of a sample that can be related to the dry mass distribution within cells and tissues, which is a powerful marker for biomedicine [6–8]. Generally, the 3D reconstruction requires solving an inverse problem using data acquired from multiple viewing directions, in this case by illuminating an object from different angles. These multiple projections are collected in 3D data arrays called a sinogram. At present, a projection number governs the fidelity of the reconstruction [1], as more projections can average out and suppress noise considerably [9]. However, practical requirements such as temporal resolution, power levels, or cost can constrain the experiment leading to increased noise. Additionally, reconstructions of cells in presence of cell debris or relatively thick specimens (e.g. tissues) are challenging due to the multiple scattering of light [10,11], which can also be considered as an additional source of noise.

To overcome this quality problem, noise suppression techniques are widely utilized. For x-ray computed tomography [12], the denoising application reduced the reconstruction error in a scatter corrected image from 10.6% to 1.7% and increased the contrast-to-noise ratio by a factor of 3.6. In the paper [13], results of a comparison of 4 different denoising techniques applied to computed tomography are presented, where the sparsity-based block-matching 3D (BM3D) [14] noise suppression provided the best results measured by SSIM metrics for the smallest number of projections. Another application of BM3D and its descendant, BM4D [15], developed for the volumetric data processing is demonstrated for

☆ IS was supported by the Academy of Finland (project no. 336357, PROFI 6 - TAU Imaging Research Platform), MZ/MK: The research leading to the described results was carried out within the program TEAM TECH/2016-1/4 of Foundation for Polish Science, co-financed by the European Union under the European Regional Development Fund.

* Corresponding author.
E-mail address: igor.shevkunov@tuni.fi (I. Shevkunov).
[1] http://www.cs.tut.fi/sgn/imaging/
[2] ORCID: 0000-0003-1507-3280
[3] ORCID: 0000-0002-4802-1105
[4] ORCID: 0000-0001-6521-6951
[5] ORCID: 0000-0002-8135-1085

https://doi.org/10.1016/j.optlaseng.2022.107228
Received 16 February 2022; Received in revised form 22 June 2022; Accepted 12 August 2022

ODT in [16], where these BM filters perform better than the traditional median filter.

The BM3D filter is one of the most popular and effective noise suppression techniques for imaging. However, BM3D is developed for real-valued images and is not as effective for complex-domain images. Recently, complex-domain (CDID) and complex cube (CCF) filters were developed [17,18]. In CDID, additionally to traditional block-matching, the filter takes into account correlations of amplitude and phase pairs for more efficient noise suppression. CCF filter, developed for hyperspectral (HS) data processing, is based on singular value decomposition (SVD) and CDID. In addition to correlations of amplitude and phase (taken into account by CDID) CCF also employs correlations between neighboring spectral channels which provides an additional advantage for denoising. For example, it is demonstrated in [19] that a sufficient improvement of spectral object detection from HS data is obtained after CCF denoising.

Similar to HS imaging, where data is collected in 3D cubes, ODT also employs a complex-valued 3D stack of projections prior to image reconstruction, and therefore CCF might be applied for denoising of ODT sinograms. However, ODT sinograms differ from HS data and CCF needs to be adjusted for better performance. In the present paper, we tune CCF for signal processing of ODT data, demonstrate the advantages of such an approach, and compare its performance to traditional and state-of-the-art denoising techniques.

The paper organized as follows. Section 2 describes a problem formulation and assumptions needed for its solution. In Section 3 the proposed denoising algorithm and its framework are presented. In Section 4 we present simulations for algorithm tuning (Subsection 4.1) applied to ODT sinograms in different noise conditions. In Section 5 we show results of ODT 3D refractive index imaging in simulations (Subsection 5.1) and experiments (Subsection 5.2), where images are reconstructed from noisy and filtered data. Final conclusions are in Section 6.

2. Problem formulation

Optical diffraction tomography is an approach to an inverse problem of reconstructing 3D scattering potential distribution $f(x,y,\alpha)$ from the multiple scattered field measurements [20]. Let $U(x,y,\alpha) \subset \mathbb{C}^{N\times M}$ be such a measurement. Each scattered field is generated by illuminating the object with the plane wave, with either object rotation or illumination tilt, varying the angle (α) between consecutive measurements.

$$U(x,y,\alpha) = U_0(x,y,\alpha) + U_s(x,y,\alpha) \tag{1}$$

where U_0 - plane wave illumination and U_s - scattered component. Under the Rytov approximation, we can express the scattered component U_s in the form of the so-called complex phase [21]:

$$\Phi_s = \ln\left(\frac{U}{U_0} + 1\right) \tag{2}$$

resulting in

$$U_s = U_0 \ln\left(\frac{U}{U_0} + 1\right) \tag{3}$$

In practice, complex field U is retrieved using 2 holograms - one captured with the measured object present in the system and the second without any objects in the field of view, which allows to compensate for systematic errors, such as systems' optical aberrations. Complex amplitudes are often retrieved from the off-axis holograms using Fourier transform method [22]. The scattering potential $f(x,y,\alpha)$ is related to the RI distribution, $n(x,y,\alpha)$, by

$$f(x,y,\alpha) = k_m^2\left[\left(\frac{n(x,y,\alpha)}{n_m}\right)^2 - 1\right] \tag{4}$$

where $k_m = \frac{2\pi n_m}{\lambda}$ and n_m is RI of a surrounding medium. We reconstruct the Fourier spectrum of the scattering potential $f(x,y,\alpha)$ by mapping 2D spectra of the complex phases $FT[\Phi_s]$ onto spherical surfaces (called Ewald's spheres) in $FT[f(x,y,\alpha)]$. The radius of the spheres is determined by the illumination wavelength λ and their positions in the 3D spectrum are determined by illumination vectors.

Stack of complex fields $U(x,y,\alpha)$ for different illumination angles are collected in a sinogram $Q_\alpha(x,y) = \{U(x,y,\alpha),\ \alpha \subset A\}$, $Q_\alpha \subset \mathbb{C}^{N\times M\times L_A}$. The whole sinogram is composed of a set of the slices A with the number of individual angles L_A. Thus, the total size of the sinogram is $N \times M \times L_A$ pixels. Then, the observations of the sinogram denoising problem under the additive noise assumption may be written as:

$$Z_\alpha(x,y) = Q_\alpha(x,y) + \varepsilon_\alpha(x,y), \tag{5}$$

where $Z_\alpha, Q_\alpha, \varepsilon_\alpha \subset \mathbb{C}^{N\times M\times L_A}$ represent the recorded noisy sinogram, clean sinogram and additive noise, respectively. Spatial coordinates (x,y) are integer numbers belonging to ranges $[1:N]$ and $[1:M]$, respectively. Accordingly to the notation for the clean sinogram, the noisy sinogram can be represented as $Z_\alpha(x,y) = \{Z(x,y,\alpha), \alpha \in A\}$, $Z_\alpha \subset \mathbb{C}^{N\times M\times L_A}$ with the slices $Z(x,y,\alpha)$. The denoising problem is formulated as a reconstruction of unknown $Q_\alpha(x,y)$ from the given $Z_\alpha(x,y)$. The properties of the clean sinogram $Q_\alpha(x,y)$ and the noise $\varepsilon_\alpha(x,y)$ are essential for the algorithm development. For the noise filtering, we exploit the following three natural properties of the model [18].

1. The sinogram slices $U(x,y,\alpha)$ for nearby angles α are similar. The similarity follows from the fact that slices $U(x,y,\alpha)$ are slowly varying functions of α. Therefore, there is a linear transform E reducing the size of the sinogram $Q_\alpha(x,y)$ to the sinogram of the smaller size in the third dimension. A smaller size of this subspace automatically means a potential to improve the denoising being produced in this smaller subspace.
2. The sinogram slices $U(x,y,\alpha)$ as functions of (x,y) are sparse. The sparsity is one of the natural and fundamental assumptions for the design of modern image processing algorithms. For complex-valued images, it is different from the real-valued signals, since complex-valued variables can be defined by any of the two pairs: amplitude/phase and real/ imaginary values and elements of these pairs are usually correlated [23].
3. The noise $\varepsilon_\alpha(x,y)$ is zero mean circular complex-valued Gaussian with real and imaginary parts uncorrelated.

We use the first property for providing principle component analysis via singular value decomposition (SVD) which provides compression of the initial noisy sinogram $Z_\alpha(x,y) \subset \mathbb{C}^{N\times M\times L_A}$ to so-called eigen-sinogram $Z_\beta(x,y) \subset \mathbb{C}^{N\times M\times L_B}$ with $L_B < L_A$. The similarity governs the L_B value: the higher the similarity the smaller the L_B. The last two model properties advocate for application of CDID filter [17], which is based on the sparsity theory and developed for additive noise. In the present paper we use CDID for noise suppression in complex-valued slices of the eigen-sinogram $Z_\beta(x,y)$. Taking into account that the first property depends on the angle steps and the object structure, it might be relaxed just by taking a smaller set of neighboring slices.

3. CCF denoising

In the publication [18] CCF is described in details, here we would like to summarize its main advantages and adaptation for tomographic data processing. CCF was developed for filtering complex-valued 3D data cubes by joint processing of its slices. In ODT neighboring projections (slices) are expected to be similar, with the similarity decreasing for the distant projections. Therefore, to process only groups of similar slices, we propose the use of CCF in a sliding window regime, which is defined by the following notation:

$$\hat{Q}(x,y,\bar{A}) = CCF\{Z(x,y,\bar{A}),\ \bar{A} \subset A\}. \tag{6}$$

Here, $\hat{Q}$ is a filtered estimate of Q, $\bar{A}$ is a set of slices to be denoised. For sliding filtering regime, $\bar{A}$ is a symmetric interval of angles centered at $\alpha = \alpha_0$ of the width $L_{\bar{A}}$:

$$\bar{A} = \{\alpha :\ \alpha_0 - L_{\bar{A}}/2 \le \alpha \le \alpha_0 + L_{\bar{A}}/2\}. \tag{7}$$

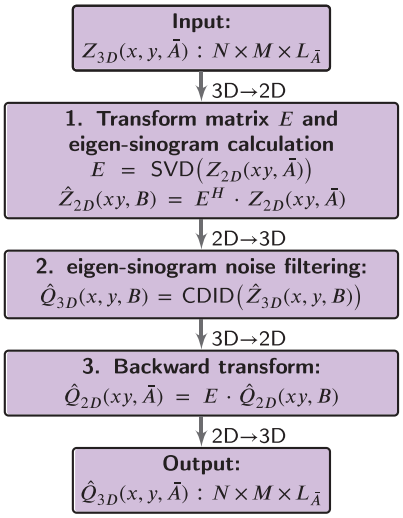

Fig. 1. CCF algorithm. Data arrays reshaping from 2D to 3D and vice versa are depicted by arrows 2D⇆3D.

Complex domain Cube Filter (CCF) processes the data of the cube $Z(x, y, \bar{A})$ jointly and provide the estimates $\hat{Q}(x, y, \bar{A})$ for all $\alpha \in \bar{A}$.

Previous investigation [18] for HS data processing shows that the CCF filtered slices $\hat{U}(x, y, \alpha)$ have the accuracy varying with α and the best results are achieved for α close to the middle point of the interval $\bar{A}$. Additionally, the degree of similarity for tomographic data is less than in HS data due to the rotation of an object during acquisition. Therefore, we utilize CCF in a sliding regime, in which a set of step-wise estimations for $\alpha = \alpha_0$ in Eq. 7 are obtained, where α_0 takes values from A. The width of the sliding window $L_{\bar{A}}$ can be varying with α_0.

As an advantage over the HS 3D data sets, scanning in ODT is usually performed in a closed loop (e.g. annular pattern around the edges of the numerical aperture), resulting in high similarity between the first and the last projection. Taking it into account, we process sinograms with an assumption of circular symmetry in the third dimension, which results in uniform noise suppression for ODT, while in HS data the CCF denoising in the neighborhood of bounding slices is worse.

Figure 1 illustrates flow chart of the CCF algorithm. It comprises of the following steps.

1. Calculation of the orthonormal transform matrix $E \subset \mathbb{C}^{L_{\bar{A}} \times L_B}$ and the 2D transform domain eigen-sinogram $Z_{2D}(xy, B)$ as

$$E = \mathrm{SVD}\big(Z_{2D}(xy, \bar{A})\big), \tag{8}$$

where SVD stays for singular value decomposition, B is a eigenspace, which length (L_B) depends on noise level and object's features. We identify L_B heuristically. When E is calculated, the eigen-sinogram is calculated as

$$\hat{Z}_{2D}(xy, B) = E^H \cdot Z_{2D}(xy, \bar{A}). \tag{9}$$

2. Filtering of each of the $N \times M$ 2D slices of $\hat{Z}_{3D}(x, y, B)$ by Complex-Domain Image Denoising (CDID) algorithm [17]:

$$\hat{Q}_{3D}(x, y, B) = \mathrm{CDID}\big(\hat{Z}_{3D}(x, y, B)\big), \tag{10}$$

where B is a subspace of eigen-sinograms and length of B is smaller than length of A.

3. Returning from the eigen-sinograms of the transform domain to the 2D original image space as follows

$$\hat{Q}_{2D}(xy, \bar{A}) = E \cdot \hat{Q}_{2D}(xy, B). \tag{11}$$

Forward and backward passages in Fig. 1 2D⇆3D signed between the algorithm steps define the reshapes from 2D to 3D and vice versa for corresponding processing of the sinogram, since SVD is developed for 2D and CDID employs spatial distribution of slices in 3D. In 3D, the coordinates are (x, y, α), and in 2D they are reshaped to (xy, α). The subscript (2D or 3D) denotes the number of dimensions.

These reshapes are needed to produce SVD transform since it works only on 2D data, but CDID filtering works in the 3D domain slice-by-slice. However, to return these filtered data to the original image space we need to use 2D transform (Eq. 11) and reshape the data back to 2D space. Optimization in step 1 results in reduced sinogram size and usually the obtained subspace dimension is much smaller than the initial one $L_B \ll L_{\bar{A}}$. This leads to a shorter processing time of the algorithm. Thus, the CDID filtering is produced only for L_B slices of the eigen-sinogram but the backward transform (Eq. 11) gives the estimates for all $L_{\bar{A}}$ slices of the original sinogram.

Figure 2 illustrates the CCF processing at each step of the algorithm, the left column shows amplitudes and the right one - phases. The input noisy sinogram $Z_{3D}(x, y, \bar{A})$ is in Fig. 2(a); the noisy eigen-sinogram $\hat{Z}_{3D}(x, y, B)$ is in Fig. 2(b), consisting only from 4 slices; the CDID filtered eigen-sinogram $\hat{Q}_{3D}(x, y, B)$ is in Fig. 2(c); and the resulting filtered sinogram $\hat{Q}_{3D}(x, y, \bar{A})$ is in Fig. 2(d). From the eigen-sinogram in Fig. 2(b) it appears that the noise is already suppressed in the first slices of amplitude and phase ($\beta = 1$), however other slices are noisy, and only after CDID filtering (see Fig. 2(c)) all eigen-sinogram slices are denoised and show clear structure. It is an essential step for denoising, otherwise the remaining noise will be spread over the whole sinogram, it is the case in the traditional principal component analysis approach [25].

4. Simulations

For the investigation of CCF tuned parameters, we perform simulations of different noise conditions with the noise model in accordance with Eq. 5. As an object under investigation, we used a numerical twin of a biological cell phantom, see Fig. 3 [24], that was later fabricated and measured using ODT system. It includes following test features: the USAF-like resolution test chart of high refractive index contrast along the X, Y, and Z axes (labeled regions 1 and 3 in Fig. 3), three spherical nucleoli suspended in a region of lower RI (nucleus, label 2) and a cylinder with radial gradient of the RI that represents slow, natural RI changes within cells (labeled region 4). These features were designed to

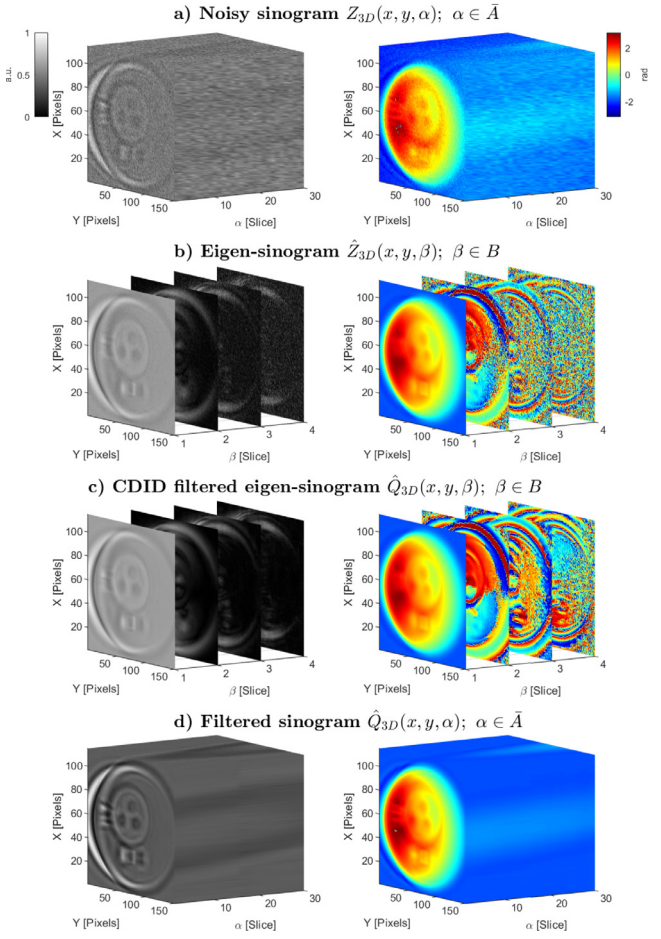

Fig. 2. Illustration of CCF algorithm processing steps. Pannels correspond to the sinogram processing steps of the algorithm. The left column shows amplitudes and the right column shows phases. (a) Input noisy sinogram consisting of 30 slices; (b) noisy eigen-sinogram after SVD consisting of 4 slices; (c) CDID filtered eigen-sinogram; (d) CCF filtered sinogram.

test the performance of the ODT and enable a comparison of numerical and experimental results. Thus, it is appropriate for benchmarking the performance of the CCF filtering under realistic conditions. A synthetic sinogram generation is based on the forward model of Fourier Diffraction Theorem. Polar illumination angle was 50° for 360 projections arranged in annular scanning pattern with 1° azimuthal step. Projections have been band limited to match a numerical aperture of the imaging objective of NA = 1.3. The illumination wavelength was $\lambda = 632.8$ nm.

We cover a wide range of sinogram signal-to-noise ratios (SNR) of [1.7 : 24.4] dB controlled by the additive noise standard deviation, σ:

$$\varepsilon(x,y,\alpha) = \frac{\sigma}{\sqrt{2}} \cdot \left(\varepsilon_{Re}(x,y) + i \cdot \varepsilon_{Im}(x,y)\right), \alpha \in A \tag{12}$$

where $\varepsilon_{Re}(x,y)$ and $\varepsilon_{Im}(x,y)$ are zero-mean independent Gaussian random variables with variance $\frac{\sigma^2}{2}$ for the noise real and imaginary parts, respectively. SNR is defined as the averaged squared amplitude of a sinogram and divided by the variance of the system noise:

$$\mathrm{SNR} = 10\log_{10}\left(\frac{\sum_{x,y,\alpha}|Z(x,y,\alpha)|^2}{\sigma^2 \cdot N \cdot M \cdot L_A}\right). \tag{13}$$

The noise suppression quality is estimated as Relative Root-Mean Square error (RRMSE) between the noiseless φ_o and filtered $\hat{\varphi}_o$ object's phases:

$$\mathrm{RRMSE} = \frac{\|\varphi_o - \hat{\varphi}_o\|_F}{\|\varphi_o\|_F}, \tag{14}$$

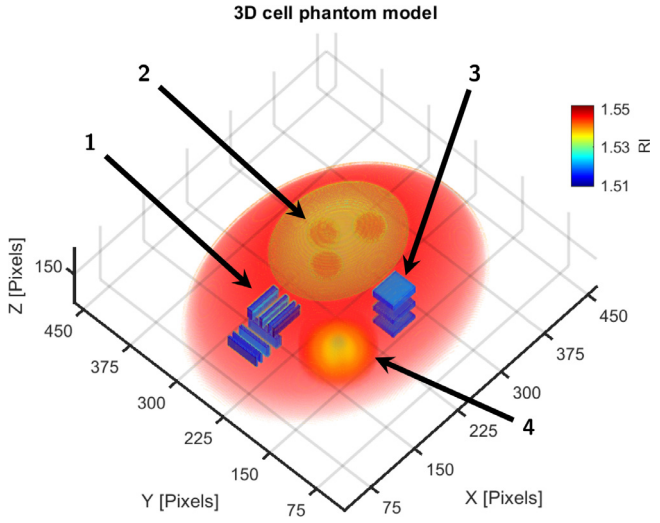

Fig. 3. Numerical model of the cell phantom. Within the truncated ellipsoid there are several test targets including resolution lines, gradient region and ellipsoid containing spheres representing 3 nucleoli suspended in nucleus. Size, morphology and ΔRI values mimic the real cell suspended in the culture medium. Maximum external dimensions in the XY plane equal 345 × 300 voxels and the height is 126 voxels. Labeled regions are: 1 - resolution lines in the X and Y directions (line widths: 3, 5 and 7 voxels, ΔRI= 0.03); 2 - spherical nucleoli (30 voxels in diameter) suspended in the low-RI region, representing the nucleus (ΔRI= 0.015); 3 - resolution lines in the Z direction (line heights: 9, 12 and 15 voxels, ΔRI= 0.03); 4 - cylinder with a radial RI gradient (ΔRI= 0.015). Sampling is typical for ODT, isotropic, equal to 100 nm/voxel [24].

Table 1
Mean RRMSE of filtered sinogram's phase depending on the eigen subspace length, L_B, and on SNR of the noisy sinogram.

L_B/SNR	24.4 dB	18.4 dB	14.1 dB	3.0 dB	1.7 dB
1	0.0381	0.0381	0.0381	0.0387	0.0392
2	0.0125	0.0126	0.0127	0.0156	0.0176
3	0.0066	0.0068	0.0072	0.0134	0.0173
4	0.0042	0.0047	0.0054	0.0135	0.0174
5	0.0031	0.0038	0.0048	0.0136	0.0174
6	0.0026	0.0034	0.0047	0.0137	0.0176

where $\|\cdot\|_F$ means the Frobenius norm. The sinogram RRMSE is estimated as averaged RRMSE of all sinogram's slices.

4.1. CCF parameters

For better performance of the CCF algorithm, we make a fine tunning of its parameters (eigen subspace length (L_B), sliding window width ($L_{\bar{A}}$), and sliding window step). Eigen subspace length (L_B) estimation is a crucial first step of the CCF algorithm since it governs the number of eigen-sinogram slices to be filtered. For this purpose, we investigated filtering of noisy sinograms in SNR range of [1.7:24.4] dB by sliding CCF with different eigen subspace length, L_B. In Table 1 we provide filtered sinogram RRMSE values depending on the eigen subspace length, L_B, and on SNR of the noisy sinogram.

For small noise cases of SNR > 14 dB, the growing L_B provides better filtering results, however for more noisy cases (SNR < 14 dB) the growing L_B does not improve filtering and, having values bigger than 4, even harms it. It happens because in high noise levels the needed similarity property for sinogram slices is not fulfilled. Therefore, we take $L_B = 4$ as the optimal value for filtering, since it provides small RRMSE in the less noisy cases and does not harm more noisy ones.

Next, to work in the sliding regime, the estimation of the sliding window width, $L_{\bar{A}}$, and sliding step is needed. For this purpose sinogram RRMSE depending on the width, $L_{\bar{A}}$, and on the step of the sliding win-

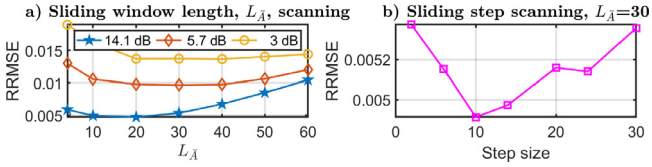

Fig. 4. CCF sliding window length, $L_{\bar{A}}$, and step choice by mean RRMSE of filtered phase sinograms. (a) Filtered sinogram RRMSE curves for noisy sinograms with SNR=3 dB (orange circles curve), SNR=5.7 dB (orange diamonds), and SNR=14.1 dB (blue stars). (b) Filtered noisy sinogram RRMSE curve for different steps of sliding window $\bar{A}$ with length $L_{\bar{A}} = 30$, SNR=14.1 dB.

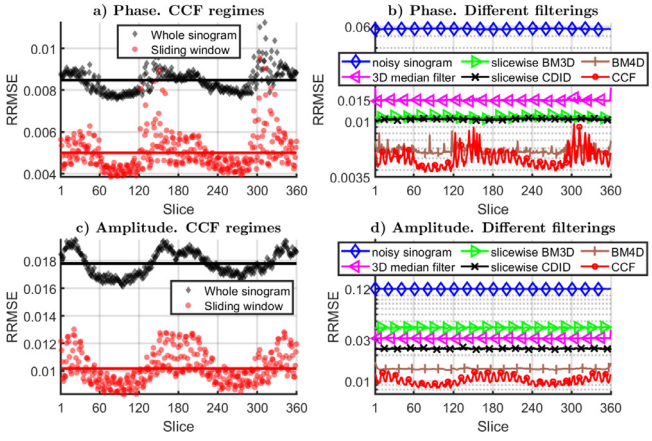

Fig. 5. (a,c) Slice-wise RRMSE for CCF filtered noisy sinogram (SNR=14 dB): black diamonds are for CCF applied for the whole sinogram, red circles are for sliding window CCF, solid curves are for mean RRMSE values. (b,d) RRMSE plots for different denoising algorithms applied for filtering. RRMSE of noisy sinogram is in blue diamonds, and filtered sinograms by: 3D median filter (purple left triangles), slicewise BM3D (green right triangles), slicewise CDID (black crosses), BM4D (brown sticks) and CCF (red circles).(a,b) is for phase, (c,d) is for amplitude.

dow for CCF is shown in Fig. 4(a) and (b), respectively. It is intuitively expected that for small values of $L_{\bar{A}}$ the noise suppression will be less effective than for the big ones, however with the limited similarity of the sinogram slices $Z(x, y, \bar{A})$ the big length of $\bar{A}$ will also be harmful. We show in Fig. 4(a) three sinogram RRMSE curves with different noise levels of 3 dB, 5.7 dB, and 14.1 dB for yellow circles, orange diamonds, and blue stars curves, respectively. All presented curves have local minimums, and with the growing noise level, the mimimum shifts to the bigger sliding window length, $L_{\bar{A}}$. To optimize performance across noise levels we choose $L_{\bar{A}} = 30$, which provides the best RRMSE value for the noisiest case, and relatively good RRMSEs for cleaner data. Due to the lower degree of similarity between distant projections (here more than 30 slices), they are not similar enough for the correct SVD processing and, therefore, for successful noise suppression.

In Fig. 4(b) the RRMSE curve for different step values for sliding window is plotted, the step values were varying inside the range $[2 : \text{length}(\bar{A})]$. The curve demonstrates that, contrary to the HS data [18], the CCF filtering of the tomographic sinograms is irrelevant to sliding step and step might be taken the same as the length of the sliding window, $L_{\bar{A}}$.

After the parameters are chosen we provide a justification of CCF filtering applied in the sliding regime against the single CCF application for the whole sinogram. For the latter case we took $L_B = 28$, which equals to the number of steps in sliding regime multiplied on the sliding $L_B = 4$. In Fig. 5(a,c) RRMSE filtering results for each slice of the noisy sinogram with SNR=14.1 dB are provided for phase and amplitude, respectively. The black diamond dots correspond to the single CCF application, red circles to the sliding CCF, and the solid lines with the corresponding colors indicate sinogram mean RRMSE. It is shown that sliding mode CCF is performing better with lower values of RRMSE.

For a comparison of CCF filtering performance with different filtering techniques we show in Fig. 5(b,d) slice-by-slice RRMSEs of filtered sinograms by: slice-wise BM3D (green right triangles curve), slice-wise CDID (black crosses curve), three-dimensional median filter with [3,3,3] kernel (purple left triangles curve), BM4D (left triangles curve), and by sliding window CCF (red circles curve). Blue diamonds curve correspond to RRMSEs of the noisy sinogram prior to filtering, SNR=14.1 dB. Fig. 5(b) is for phase and (d) is for the amplitude. It is demonstrated that slice-wise filtering techniques are performing worse than BM4D and CCF, which use 3rd dimension for denoising. However, because of consideration of phase-amplitude correlations CCF performs better than BM4D and the lowest RRMSE values for CCF confirm its high noise suppression performance.

For simulations we used MATLAB R2020b environment on a computer equipped with 32 GB of RAM and 3.40 GHz Intel®Core™ i7-3770 CPU. The computation complexity of the algorithm is characterized by the time required for processing. For the $280 \times 280 \times 360$ complex-domain sinogram, filtering by CCF takes 2780 seconds, among which 2700 is spent by CDID. With some optimization and utilization of the GPU acceleration [26], we expect that this time might be decreased at least 100 fold.

We make the MATLAB demo codes (see Supplementary code) of the developed CCF algorithm publicly available. These can be used to reproduce the experiments presented in this paper as well as for further tests.

5. Results

Original, noisy and denoised synthetic sinograms, followed by the experimental sinograms were reconstructed in order to ascertain the impact of the denoising on the 3D RI distribution. For this purpose we used a direct inversion algorithm (DI) [27] under the first-order Rytov approximation [28,29]. The algorithm is a straightforward implementation of the generalized projection theorem [20] and applies direct interpolation of the object beam information into the 3D spectrum of the sample. We chose this reconstruction method because of its current popularity in ODT, robustness, and short computation time.

5.1. Simulation results

For the demonstration of a CCF filtering performance and improvements in ODT, in this section, we show images of noiseless sinogram (Fig. 6 a,d), noisy sinogram (b,e) with SNR=5.7 dB, and CCF filtered noisy sinogram (c,f). The top row is for whole data cubes and the bottom row illustrates the typical sinogram appearance as 2D section of the 3D data cube in (x, α) plane for $Y = 100$. As can be seen in Fig. 6(c,f) that noise is suppressed, CCF filtered sinogram corresponds to the noiseless one, and low RRMSE=0.021 value indicates high quality filtering with preservation of sinogram's details, as demonstrated in the following reconstructions.

ΔRI images presented in Fig. 7 are reconstructed from the given noiseless sinogram Fig. 7(a,b,c), from the noisy sinogram, SNR=5.7 dB Fig. 7(d,e,f), from the 3D median filtered noisy sinogram Fig. 7(g,h,i), from BM4D filtered noisy sinogram Fig. 7(j,k,l), and from CCF filtered noisy sinogram Fig. 7(m,n,o). Panels (p,q,r,s) in Fig. 7 provide cross-sections for the corresponding planes marked in panels (a,b,c) as dash-dot green lines. Scale bar in images equals to 5 μm. Observing the empty spaces of reconstruction from filtered sinograms by all filters, it is clear that all filtering techniques provide noise suppression and filtered images are less noisy. However, the 3D median filtered images lose high

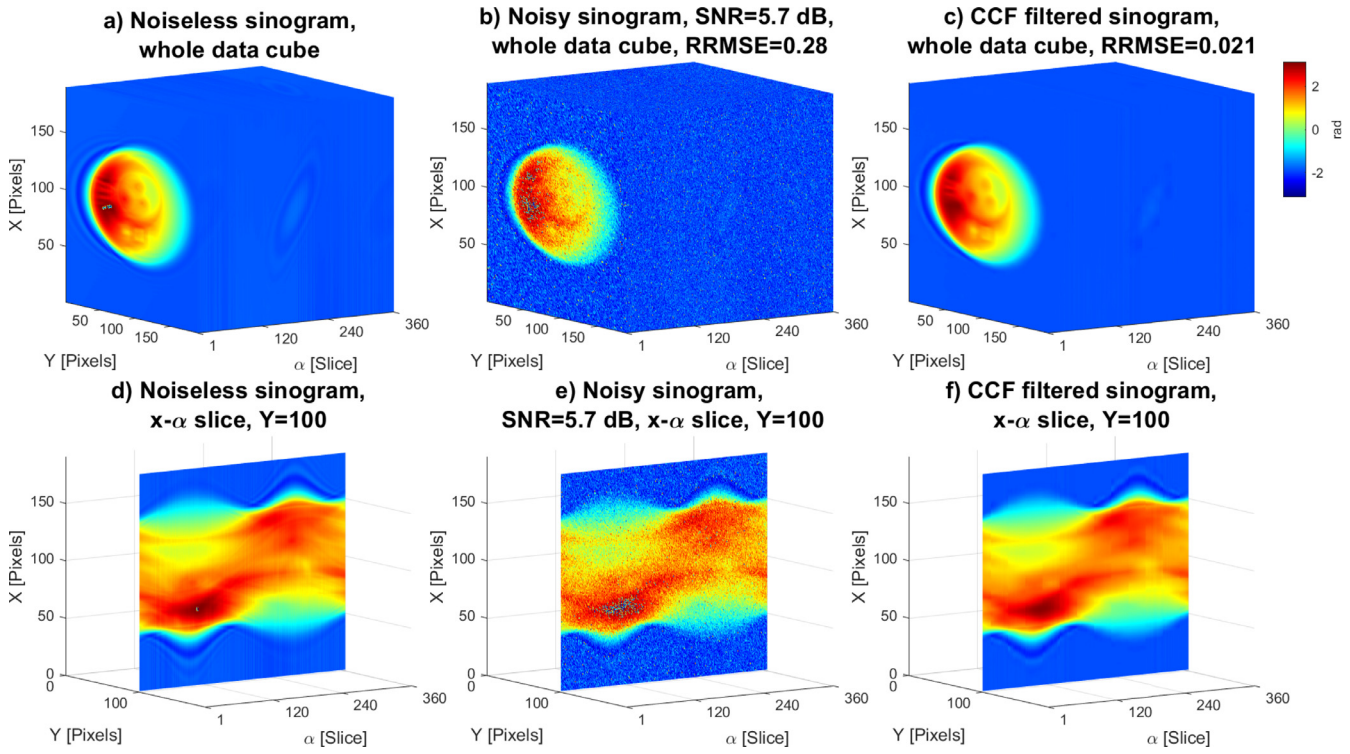

Fig. 6. Images of phase sinograms: noiseless (a,d), noisy with SNR=5.7 dB (b,e), CCF filtered noisy sinogram (c,f). The top row shows the whole data cubes, while the bottom row shows the single slice at Y=100.

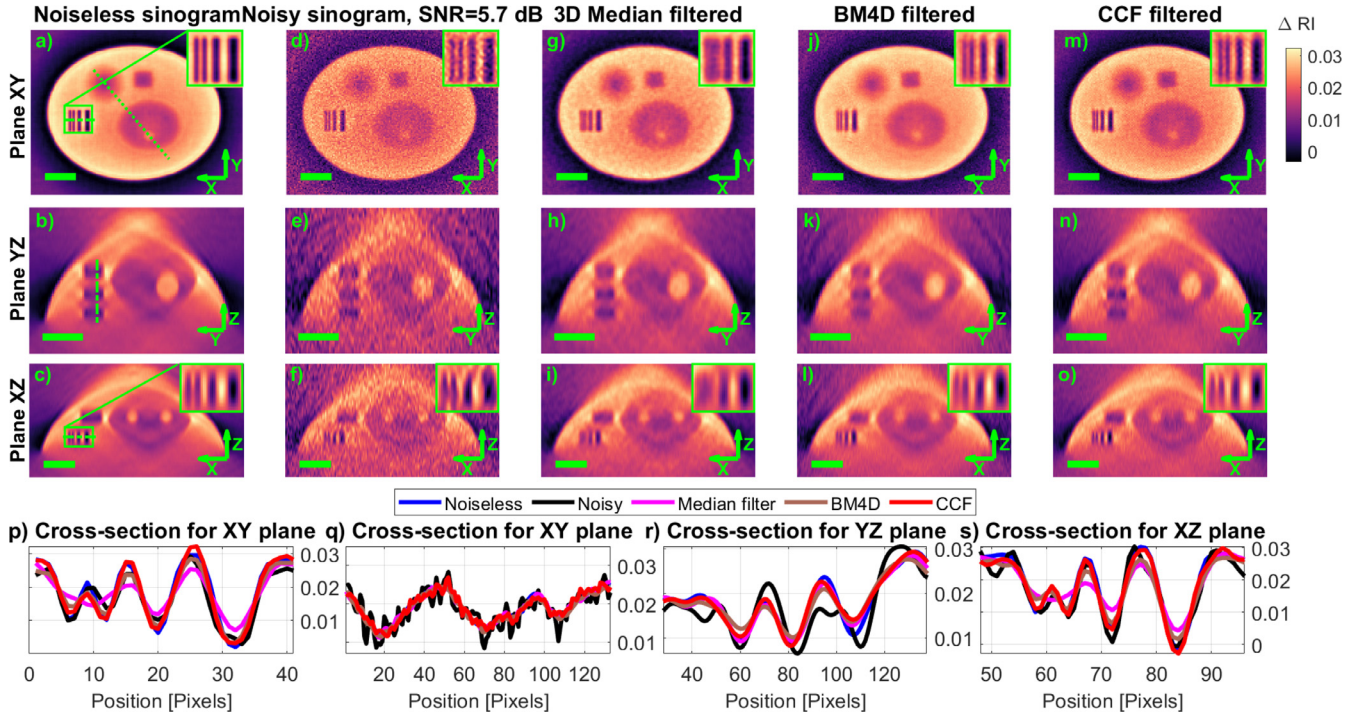

Fig. 7. Simultated ΔRI reconstructions from noiseless sinogram (a,b,c), from noisy sinogram with SNR=5.7 dB (d,e,f), from 3D median filtered noisy sinogram (g,h,i), from BM4D filtered noisy sinogram (j,k,l), and from CCF filtered noisy sinogram (m,n,o). The top row shows XY plane, the second row - YZ plane, and the third row - XZ plane. Dash dot lines in (a,b,c) show cross-sections locations for the corresponding planes. Cross-sections from all reconstructions are presented in subplots (p,q,r,s) for XY horizontal line, XY 45° angled line, YZ, and XZ planes, respectively. Scale bar is 5μm. Filtering results for the whole cell by CCF can be found in the supplementary Visualization 1.

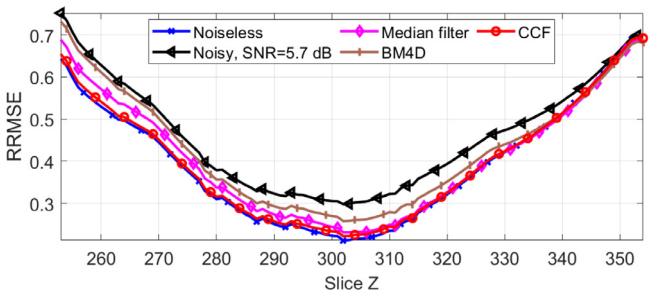

Fig. 8. RRMSE curves for reconstructions of cell phantom from: noiseless sinogram (blue crosses curve), noisy sinogram with SNR=5.7 dB (black left triangles), and noisy sinogram filtered by 3D median filter (purple diamonds), by BM4D (brown sticks), and by CCF (red circles).

frequency details and provide blurry reconstructions. BM4D demonstrates better quality in terms of resolution, but lacks noise suppression of surrounding media of the phantom. CCF filtered images demonstrate, along with the suppressed noise of the surrounding media, high resolution and contrast when compared to the reconstruction from the noiseless sinogram. In cross-sections Fig. 7(p,q,r,s) blue curves correspond to noiseless reconstruction, black to noisy, purple to 3D median filtered, brown to BM4D filtered, and red to CCF. In each plane CCF cross-section curves are the closest to the cross-sections from the noiseless sinogram reconstruction.

In terms of RRMSE, the reconstruction quality is demonstrated in Fig. 8 where slice-wise RRMSE is provided for each filtering technique. X-axis is for Z slice of the reconstruction, where the starting slice Z=254 is for the top of the phantom and Z=354 is for the bottom. RRMSE of phantom reconstruction from the noiseless sinogram is plotted using the blue crosses curve, from noisy sinogram with SNR=5.7 dB - black left triangles, from noisy sinogram filtered by 3D median filter - purple diamonds, by BM4D - brown sticks, and by CCF - red circles. Again, CCF demonstrates the closest RRMSE values to the noiseless reconstruction which indicates the highest quantitative quality among the considered filters. It is interesting to note that BM4D performance in RRMSE values for sinograms was better than for the 3D median filter (see Fig. 5), however in the final reconstruction BM4D performs worse, which is caused by worse noise suppression in the surrounding media, see plane YZ in Fig. 7 (h,k,n).

5.2. Experimental results

For experimental demonstration of CCF filtering we have captured noisy sinogram of the 3D-printed cell phantom with the 3D RI distribution corresponding to the simulated one, shown in Fig. 3. It has been manufactured by 3D laser photolithography (direct laser writing) and described in detail in [24]. External dimensions are $30 \times 25 \times 11\,\mu$m, with the smallest features (resolution test lines) being as small as 300 nm. The ODT system is based on the Mach-Zehnder interferometer also described in [24]. Briefly, the laser beam (633 nm wavelength) is split in two paths. The object beam is steered by the dual-axis galvanometer mirrors and illuminates the sample (coverslip with the phantom immersed in Zeiss Immersol 518F immersion oil) from various directions as in the simulations - annular pattern at 50° polar angle in the sample plane. The diffraction pattern is captured by the x40, 1.3NA microscope objective and relayed onto the camera, where the object beam recombines with the reference beam. The resulting off-axis holograms for each of the 180 illumination angles are demodulated using the Fourier transform method providing amplitude and phase sinograms. In order to increase the noise level in the system, we introduced additional coverslip covered in dust and fingerprints to the object beam path, as well as lowered the camera exposure to utilize only about 30% of its 8-bit dynamic range.

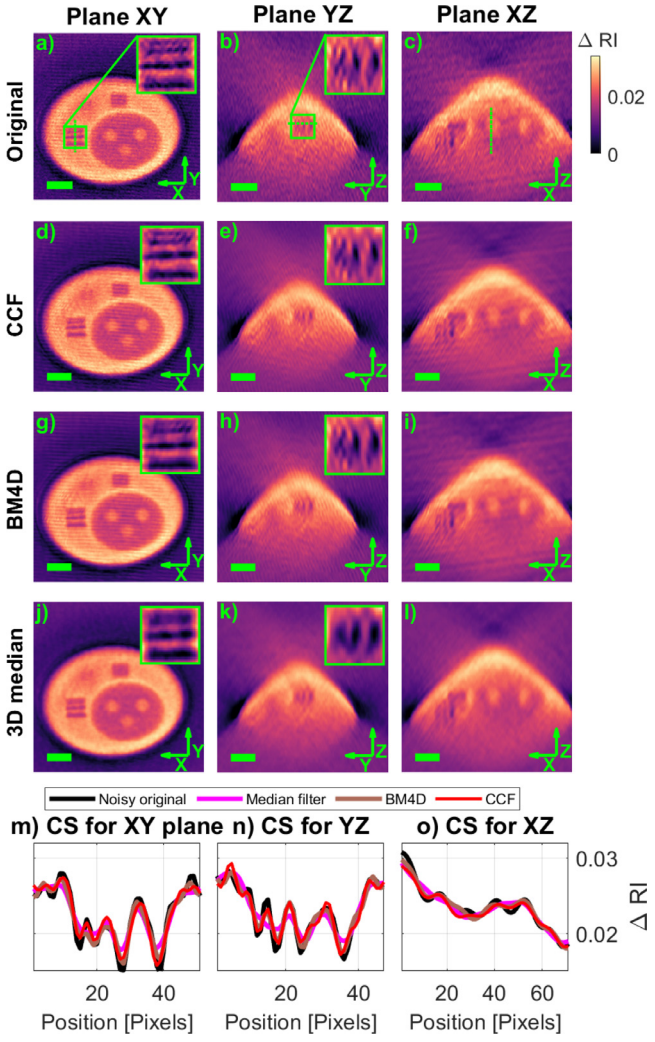

Fig. 9. Experimental ΔRI reconstructions from noisy sinogram (a,b,c), from CCF filtered noisy sinogram (d,e,f), and 3D median filtered noisy sinogram (g,h,i). The left column is for XY plane, the middle column is for XZ plane, and the right column is for XZ plane. Cross-sections from all reconstructions are presented in subplots (j,k,l) for XY, XZ, and YZ planes, respectively. In cross-section plots black triangles curve is for reconstruction from noisy sinogram, red circles curve is for filtered by 3D median filter, and blue crosses curve is for CCF filtered. Scale bar is 5 μm. Filtering results for the whole cell by CCF can be found in the supplementary Visualization 2.

This results in the SNR of 22.9 dB, estimated [30] in the object-free region of the sinogram.

In Fig. 9 we show experimental ΔRI reconstructions of the cell phantom from original noisy sinogram (a,b,c), from CCF filtered noisy sinogram (d,e,f), from BM4D filtered noisy sinogram (g,h,i), and 3D median filtered sinogram (j,k,l). Cross-sections from original noisy sinogram (black), and filtered sinograms by CCF (red), BM4D (brown), and 3D medial filtered (pink) are presented in Fig. 9(m,n,o) for XY, YZ, and XZ planes, respectively. Similarly as in the simulations, all presented filters demonstrate reliable noise suppression. However, in reconstruction using 3D median filter resolution has significantly dropped and high frequency object details are lost. Comparing BM4D and CCF, especially using the zoomed insets and cross-sections, it is clear that CCF provides better resolved details and close values to the reconstruction from the original sinogram. Additionally, CCF better suppresses structured noise in the surrounding media of the cell-phantom, which is clearly seen in Plane XZ in Fig. 9.

6. Conclusion

We have demonstrated a successful application of the complex-domain cube filter (CCF) for noise suppression in 3D complex-valued data of optical diffraction tomography (ODT). Because of the particular projection preprocessing in ODT, CCF is tuned accordingly for better performance. CCF is based on two processing steps, the first is singular value decomposition (SVD), and the second is complex-domain sparsity filter (CDID). While SVD provides data compression and initial denoising, CDID employs sparsity theory and phase-amplitude correlation to make a precise denoising in the compressed domain. ODT sinograms have a low order of similarity, and we found that CCF filter provides better results when running in a sliding regime, where the sinogram advantage for noise suppression is the similarity of the first and last slices of the sinogram, therefore noise suppression is uniform along the whole sinogram. We have shown in simulations and experiment that CCF improves the precision of the refractive index reconstruction and retrieves object's details even for highly noisy data. Enhanced resolution and quantitative ODT estimations are essential for precise medical diagnostic [31,32]. With the trends of automatization, demonstrated noise suppression in surrounding media (outside the investigated object) will provide a better image segmentation which will result in simpler and robust object recognition [33,34]. Additionally, CCF enables tomographic imaging with lower exposure times, which will result in the shortening of the recording process. Going outside the visible range of illumination, in X-ray tomography, radiation doses might be decreased with the same quality imaging, which is essential for patient's health [35]. These advantages are vital for specific applications of ODT and for facilitating their transition from optical and imaging laboratories to biomedical and diagnostic facilities.

Credit Author Statement

Igor Shevkunov is responsible for algorithm development, simulations, data processing, paper writing.

Michał Ziemczonok is responsible for ODT experiments, data processing, and paper writing.

Małgorzata Kujawińska: supervising the project.

Karen Egiazarian: supervising the project.

Competing interests

Michał Ziemczonok and Małgorzata Kujawińska are named inventors on the patent related to the cell phantom design. Igor Shevkunov and Karen Egiazarian declare no competing interests.

Declaration of Competing Interest

The authors declare the following financial interests/personal relationships which may be considered as potential competing interests:

Michal Ziemczonok, Kujawinska Malgorzata has patent #P.429994 (PL, granted) issued to Warsaw University of Technology. Michal Ziemczonok, Kujawinska Malgorzata has patent #PCT/IB2020/054772 (PCT application) pending to Warsaw University of Technology.

Supplementary material

Supplementary material associated with this article can be found, in the online version, at 10.1016/j.optlaseng.2022.107228

References

[1] Hsieh J. Computed tomography: principles, design, artifacts, and recent advances, vol 114. SPIE press; 2003.

[2] Maire E, Withers PJ. Quantitative X-ray tomography. Int Mater Rev 2014;59(1):1–43. doi:10.1179/1743280413Y.0000000023.

[3] Parasu Veera U. Gamma ray tomography design for the measurement of hold-up profiles in two-phase bubble columns. Chemical Engineering Journal 2001;81(1–3):251–60. doi:10.1016/S1385-8947(00)00202-3.

[4] Mittleman DM, Hunsche S, Boivin L, Nuss MC. T-Ray Tomography. In: Ultrafast Electronics and Optoelectronics. Washington, D.C.: OSA; 1997. p. UF5. ISBN 1-55752-486-6.

[5] Sung Y, Choi W, Fang-Yen C, Badizadegan K, Dasari RR, Feld MS. Optical diffraction tomography for high resolution live cell imaging. Opt Express 2009;17(1):266. doi:10.1364/OE.17.000266.

[6] Liu PY, Chin LK, Ser W, Chen HF, Hsieh CM, Lee CH, et al. Cell refractive index for cell biology and disease diagnosis: past, present and future. Lab Chip 2016;16(4):634–44. doi:10.1039/c5lc01445j.

[7] Park Y, Depeursinge C, Popescu G. Quantitative phase imaging in biomedicine. Nat Photonics 2018;12(10):578–89. doi:10.1038/s41566-018-0253-x.

[8] Balasubramani V, Kuś A, Tu H-Y, Cheng C-J, Baczewska M, Krauze W, et al. Holographic tomography: techniques and biomedical applications [Invited]. Appl Opt 2021;60(10):B65. doi:10.1364/AO.416902.

[9] Belashov AV, Petrov NV, Semenova IV. Accuracy of image-plane holographic tomography with filtered backprojection: random and systematic errors. Appl Opt 2016;55(1):81. doi:10.1364/AO.55.000081.

[10] Chen H, Fu S, Wang H, Wang H, Li Y, Wang F. Speckle reduction based on fractional-order filtering and boosted singular value shrinkage for optical coherence tomography image. Biomed Signal Process Control 2019;52:281–92. doi:10.1016/j.bspc.2019.04.033.

[11] Yoon S, Kim M, Jang M, Choi Y, Choi W, Kang S, Choi W. Deep optical imaging within complex scattering media. Nature Reviews Physics 2020;2(3):141–58. doi:10.1038/s42254-019-0143-2.

[12] Zhu L, Wang J, Xing L. Noise suppression in scatter correction for cone-beam CT. Med Phys 2009;36(3):741–52. doi:10.1118/1.3063001.

[13] Trinh H. An optimal weight method for CT image denoising. J Electron Sci Technol 2012;10(2). https://www.researchgate.net/publication/230695454.

[14] Dabov K, Foi A, Katkovnik V, Egiazarian K. Image denoising by sparse 3-D transform-domain collaborative filtering. IEEE Trans Image Process 2007;16(8):2080–95. doi:10.1109/TIP.2007.901238.

[15] Maggioni M, Katkovnik V, Egiazarian K, Foi A. Nonlocal transform-domain filter for volumetric data denoising and reconstruction. IEEE Trans Image Process 2013;22(1):119–33. doi:10.1109/TIP.2012.2210725.

[16] Stepien P, Kujawińska M. Block-matching-based filtration in holographic tomography reconstruction. In: Ferraro P, Ritsch-Marte M, Grilli S, Hitzenberger CK, editors. Optical Methods for Inspection, Characterization, and Imaging of Biomaterials IV. SPIE; 2019. p. 44. ISBN 9781510627994.

[17] Katkovnik V, Egiazarian K. Sparse phase imaging based on complex domain nonlocal BM3d techniques. Digital Signal Processing: A Review Journal 2017;63:72–85. doi:10.1016/j.dsp.2017.01.002.

[18] Shevkunov I, Katkovnik V, Claus D, Pedrini G, Petrov NV, Egiazarian K. Hyperspectral phase imaging based on denoising in complex-valued eigensubspace. Opt Lasers Eng 2020;127(X):1–9. doi:10.1016/j.optlaseng.2019.105973.

[19] Shevkunov I, Katkovnik V, Claus D, Pedrini G, Petrov NV, Egiazarian K. Spectral object recognition in hyperspectral holography with complex-domain denoising. Sensors (Switzerland) 2019;19(23):1–10. doi:10.3390/s19235188.

[20] Wolf E. Three-dimensional structure determination of semi-transparent objects from holographic data. Opt Commun 1969;1(4):153–6.

[21] Kak AC, Slaney M. Principles of computerized tomographic imaging. SIAM; 2001.

[22] Tahara T, Quan X, Otani R, Takaki Y, Matoba O. Digital holography and its multidimensional imaging applications: a review. Microscopy 2018;67(2):55–67. doi:10.1093/jmicro/dfy007.

[23] Katkovnik V, Ponomarenko M, Egiazarian K. Sparse approximations in complex domain based on BM3d modeling. Signal Processing 2017;141:96–108. doi:10.1016/j.sigpro.2017.05.032.

[24] Ziemczonok M, Kuś A, Wasylczyk P, Kujawińska M. 3D-Printed biological cell phantom for testing 3D quantitative phase imaging systems. Sci Rep 2019;9(1):1–9. doi:10.1038/s41598-019-55330-4.

[25] Wold S, Esbensen K, Geladi P. Principal component analysis. Chemometrics and intelligent laboratory systems 1987;2(1–3):37–52.

[26] Davy A, Ehret T. GPU Acceleration of NL-means, BM3d and VBM3d. Journal of Real-Time Image Processing 2021;18(1):57–74. doi:10.1007/s11554-020-00945-4.

[27] Pan S, Kak A. A computational study of reconstruction algorithms for diffraction tomography: interpolation versus filtered-backpropagation. IEEE Trans Acoust 1983;31(5):1262–75.

[28] Devaney A. Inverse-scattering theory within the rytov approximation. Opt Lett 1981;6(8):374–6.

[29] Kuś A, Krauze W, Makowski PL, Kujawińska M. Holographic tomography: hardware and software solutions for 3D quantitative biomedical imaging. ETRI Journal 2019;41(1):61–72. doi:10.4218/etrij.2018-0505.

[30] Mäkitalo M, Foi A. Noise parameter mismatch in variance stabilization, with an application to poisson–gaussian noise estimation. IEEE Trans Image Process 2014;23(12):5348–59. doi:10.1109/TIP.2014.2363735.

[31] Kim K, Yoon J, Shin S, Lee S, Yang S-A, Park Y. Optical diffraction tomography techniques for the study of cell pathophysiology. Journal of Biomedical Photonics & Engineering 2016;2(2). 020201–1

[32] Kim SY, Lee JH, Shin Y, Kim TK, Lee Jw, Pyo MJ, et al. Label-free imaging and evaluation of characteristic properties of asthma-derived eosinophils using optical diffraction tomography. Biochem Biophys Res Commun 2022;587:42–8. doi:10.1016/j.bbrc.2021.11.084.

[33] Kim T, Park J. Analyzing 3D cell data of optical diffraction tomography through volume rendering. 2018 International Workshop on Advanced Image Technology, IWAIT 2018 2018:1–4. doi:10.1109/IWAIT.2018.8369805.

[34] Ziemczonok M, Kuś A, Kujawińska M. Optical diffraction tomography meets metrology - measurement accuracy on cellular and subcellular level. Measurement 2022;195:111106. doi:10.1016/J.MEASUREMENT.2022.111106.

[35] Shaker K, Häggmark I, Reichmann J, Arsenian-Henriksson M, Hertz HM. Phase-contrast X-ray tomography resolves the terminal bronchioles in free-breathing mice. Communications Physics 2021;4(1):1–9. doi:10.1038/s42005-021-00760-8.

Igor Shevkunov is a postdoctoral researcher in Tampere University since 2017. He received his Ph.D. in Optics from St.Petersburg State University, Russia, in 2013. He is the author of more than 50 refereed papers. His main research interests are digital holography, phase retrieval, denoising, and interferometry.

Michał Ziemczonok is a Ph.D. student at Warsaw University of Technology. He is working on computational imaging and 3D quantitative phase imaging techniques, as well as metrology of these systems using bio-inspired test structures fabricated via two-photon polymerization.

Kujawińska Małgorzata SPIE Fellow, Full Professor of applied optics at Warsaw University of Technology, head of Photonics Engineering Division at Institute of Micromechanics and Photonics. Expert in full-field optical metrology and 3D imaging with special focus on holography, development of novel photonics measurement systems, data analysis for metrology and 3D displays, 3D quantitative imaging in biomedical engineering. Author of one monograph, several book chapters and more than 200 papers in international scientific journals. She is the recipient of SPIE 2013 Chandra S. Vikram Award in Optical Metrology and SPIE 2020 Denis Gabor Award in Diffractive Optics.

Karen Egiazarian received his MS.c. degree from Yerevan State University, in 1981, his PhD from Moscow State University, Russia, in 1986, and the DTech degree from Tampere University of Technology (TUT), Finland, in 1994. He is a professor leading the Computational Imaging Group, ICT faculty, Tampere University. He has authored about 650 refereed journal and conference papers. His research interests include computational imaging, sparse coding, and image and video restoration. He served as an associate editor for the IEEE Transactions of Image Processing and was the editor-in-chief of the Journal of Electronic Imaging.